Aerodynamic Noise Prediction of Strut-Braced Wing Aircraft

Sticchi, E.; Ragni, D.; Casalino, D.; Avallone, F.

DOI
10.2514/6.2024-3012

Publication date
2024

Document Version
Final published version

Published in
30th AIAA/CEAS Aeroacoustics Conference (2024)

Aeroacoustics Conferences
June 4-7, 2024, Rome, Italy
30th AIAA/CEAS Aeroacoustics Conference (2024)

10.2514/6.2024-3012

Aerodynamic Noise Prediction of Strut-Braced Wing Aircraft

E. Sticchi* and D. Ragni† and D. Casalino‡
Delft University of Technology, Flow Physics and Technology Department, Kluyverweg 1, 2629 HS Delft, Netherlands

F. Avallone§
Polytechnic University of Turin, Department of Mechanical and Aerospace Engineering, Corso Duca degli Abruzzi 24, Torino, 10129, Italy

Motivated by the potential benefit of Strut-Braced Wing (SBW) configurations in reducing fuel burn, this manuscript investigates the noise generated by the interaction between the propeller slipstream and the SBW. The flow field on a regional transport aircraft is computed in high-lift condition by means of a high-fidelity Lattice Boltzmann solver with very large eddy simulation approach. The acoustic far field is obtained using the Ffowcs-Williams and Hawkings acoustic analogy. The analysis shows that the main aeroacoustic effect due to the interaction between the SBW and the propeller slipstream is the emergency of a tonal noise scattering from the region bounded by the pressure side of the main wing and the suction side of the strut at twice the blade passing frequency.

I. Nomenclature

$\mathbf{x}$	=	Spatial coordinate vector
ρ	=	Fluid density
Δt	=	Time step
τ	=	Relaxation time
τ_{eff}	=	Effective Relaxation time
M_∞	=	Freestream Mach number
p_∞	=	Freestream pressure
q_∞	=	Freestream dynamic pressure
Re_∞	=	Freestream Reynolds number
α	=	Angle of attack
RNG	=	Re-Normalisation Group
κ	=	Turbulent kinetic energy
ϵ	=	Turbulent dissipation
VLES	=	Very Large Eddy Simulation
C_T	=	Thrust coefficient
RPM	=	Rate per minute
ℓ	=	Fuselage length

II. Introduction

With the increasing of global aviation demand, expected to quadruple between 2020 and 2050 [1], there is the needing to develop new aircraft technology and configuration limiting the fuel consumption and enabling a more

*PhD Candidate, Delft University of Technology, Faculty of Aerospace Engineering, Department of Flow Physics and Technology, Wind Energy Section, Aeroacoustics group, e.sticchi@tudelft.nl
†Associate Professor, Delft University of Technology, Faculty of Aerospace Engineering, Department of Flow Physics and Technology, Wind Energy Section, Aeroacoustics group, d.ragni@tudelft.nl, AIAA Member
‡Full Professor, Delft University of Technology, Faculty of Aerospace Engineering, Department of Flow Physics and Technology, Wind Energy Section, Aeroacoustics group, d.casalino@tudelft.nl
§Full Professor, Polytechnic University of Turin, Department of Mechanical and Aerospace Engineering, francesco.avallone@polito.it, AIAA Member

environmental friendly aviation. Indeed, to meet the decarbonization target issued by the European commission the greenhouse gas emission must be reduced of 55% by 2030 compared to 1990 [2].

A possible solution to decrease the fuel consumption of aircraft is reducing the lift-induced drag, which constitutes about 40% of the total drag during cruise [3]. This can be achieved by designing wings with higher aspect ratios. One of the most promising configurations to fulfill this objective is the Strut-Braced Wing (SBW). Indeed, compared to a cantilever wing in which the increasing of span size to reduce induced drag is constrained by structural weight [4], the strut braced can have a longer span since the strut alleviates the bending moment in the main wing. Moreover, the strut enables the reduction of the main wing thickness-to-chord ratio, which ultimately leads to a decrease of the structural weight. These advantages coupled with its compatibility with conventional fuselage and empennage design make the strut-braced wing a perfect candidate for a near-term entry into service vehicle [5].

The idea of strut-braced and truss-braced wings dates back the 50' with the pilot Maurice Hurel [6]. After the second world war, with his wind tunnel tests, he demonstrated that the induced drag of a monoplane braced was less than the one of a cantilever with the same span and area. The first practical demonstration of his ideas was the Hurel-Dubois H.D.10 [7], a research plane equipped by a strut-braced wing with an aspect ratio of 32.5-to-1. Subsequently his idea was retained by *Short Brothers* though a long series of better streamlines light transport, including the famous C-23 Sherpa extensively used by the United States Army [8]. Recently, the constant effort toward greener aviation has reawakened the interest in this type of configuration for civil transport aviation purpose. Initiatives by NASA, Boeing, ONERA, and DLR have explored the employment of the strut-braced wing at various transonic cruise Mach numbers [9–11], whereas the Clean Aviation HERWINGT project is investigating the applicability of this type of wing configuration for a propeller-driven regional-transport aircraft cruising at Mach number $M_\infty = 0.5$.

Although different number of studies have demonstrated the potential benefits of strut-braced and truss-braced wings [11–19], there is motivation for further investigations into a number of challenges that have to be addressed during the design phase, such as the interaction between the propeller wake and the strut-braced wing and the design of the strut-wing junction which is subjected to a highly complex flow field. Several effort has been made to perform the aerodynamic design of strut-braced wings [20–22], however, to the authors' knowledge, no work has been done to assess the aeroacoustics performances of this kind of aircraft configuration. This gap is significant since aircraft noise is subjected to strict regulatory standards, and manufacturers must ensure compliance with these standards. Furthermore, assessing the aeroacoustics of non-conventional aircraft configurations is essential to address the potential noise issues in order to meet the continuously stringent noise regulations [23]. Since one of the most important noise sources in propeller-driven aircraft is given by the aerodynamic interaction between the propeller slipstream and the wing, it is of importance to understand how this interaction changes in presence of an additional streamlined surface, such as the strut. Furthermore, the flow around the strut-wing junction is characterized by a primary horseshoe vortex and some secondary vortices which lead to severe pressure fluctuation [24]. These vortical structures are observed to generate noise [25, 26], and the extent of this noise might depend on the incoming flow conditions and the size of the strut. The intricate interaction between these structures, those generated on the main wing, and those originating behind a propeller, coupled with the presence of multiple surfaces, can lead to substantial noise generation. This motivates the present work in which the primary sources of noise on a propeller-driven strut-braced wing aircraft will be analysed with intent of quantify the effect of the slipstream interaction in the acoustic far-field. The flow field will be computed by means of high-fidelity Very Large Eddy Simulations (VLES) whereas the acoustic impact on the far field will be analysed through the Ffowcs Williams and Hawkings (FWH) equation.

The work is outlined as follow: the numerical methodology used is reported in Section III. Subsequently, the numerical setup is exposed in Section IV. Results obtained are presented in Section V and the main conclusion are summarized in Section VI.

III. Methodology

The flow-field has been computed using the commercial flow solver PowerFLOW®, version 6-2022-R3 from Dassault Systèmes, which implements the Lattice-Boltzmann Method (LBM). The software has been extensively used to accurately predict noise generated in complex flow problems, and more specifically for full-vehicle configurations[27–35], and for propulsive units[36–39].

In the LBM, the motion of a collection of fluid particles at *mesoscopic* level is described using distribution functions. The Boltzmann transport equation (see Eq. 1) is used to model the advection and collisions of fluid particles:

$$\frac{\partial f}{\partial t} + \mathbf{V} \cdot \boldsymbol{\nabla} f = C, \tag{1}$$

where $f(\mathbf{x}, t, \mathbf{V})$ is a probability density function representing the probability of finding, in the elementary volume $d\mathbf{x}$ around a spatial coordinate $\mathbf{x}$ and in the infinitesimal time interval $(t, t + \Delta t)$, a number of fluid particles with velocity in the interval $(\mathbf{V}, \mathbf{V} + d\mathbf{V})$. C is the collision operator which accounts for particles velocity distribution changes due to momentum exchanges during collisions. Thus, the left-hand side of Eq. (1) describes the particles advection, whereas the right-hand side describes the collision process. Eq. 1 is discretized using a Cartesian grid (i.e. lattice) as follow:

$$f_i\left(\mathbf{x} + \mathbf{V_i}\Delta t, t + \Delta t\right) - f_i\left(\mathbf{x}, t\right) = C_i\left(\mathbf{x}, t\right)\Delta t, \tag{2}$$

where f_i is the particle distribution function along the i^{th} lattice direction, V_i is the discrete particle velocity in the i^{th} direction. The collision operator C_i follows the Bhatnagar–Gross–Krook (BGK) model [40] and it is reported in Eq. 3,

$$C_i = -\frac{1}{\tau}\left[f_i\left(\mathbf{x}, t\right) - f_n^{eq}\left(\mathbf{x}, t\right)\right], \tag{3}$$

where τ is the relaxation time, which is a function of fluid viscosity and temperature, and f_n^{eq} is the equilibrium distribution function of Maxwell–Boltzmann approximated with a second-order expansion [41]. The velocity space is discretized into 19 discrete speeds (D3Q19 model), involving a third-order truncation of the Chapman-Enskog expansion. It was shown that this scheme ensures sufficient lattice symmetry to recover the Navier–Stokes equations for a perfect gas at low Mach number in iso-thermal conditions [41]. For Mach numbers larger than about 0.5, for which the flow heating due to compression work is not negligible, a non iso-thermal model is available in PowerFLOW, which consists in solving a coupled equation for the total energy. This model extends the capability of the D3Q19 scheme in the high-subsonic and transonic regime, as relevant to the present study.

After solving Eq. (2), the macroscopic flow quantities are recovered by means of the following moments of the distribution function f:

$$\rho\left(\mathbf{x}, t\right) = \sum_i f_i\left(\mathbf{x}, t\right), \quad \rho\mathbf{u}\left(\mathbf{x}, t\right) = \sum_i \mathbf{V_i} f_i\left(\mathbf{x}, t\right). \tag{4}$$

For high-Reynolds-number flows, turbulence modeling is incorporated into Eq. 2 by replacing the relaxation time by an effective turbulent relaxation time [42]:

$$\tau_{eff} = \tau + C_\mu \frac{\kappa^2/\epsilon}{\left(1 + \eta^2\right)^{1/2}}, \tag{5}$$

where $C_\mu = 0.09$ and η is a combination of local strain $\kappa|\mathbf{S}/\epsilon|$, local vorticity $\kappa|\omega/\epsilon|$ and local helicity parameters. The turbulent kinetic energy and the turbulent dissipation are obtained by solving a variant of the RNG κ-ϵ model [43]. Notice that, although the relaxation time is computed using a two-equation transport model, it is not used to compute an equivalent eddy viscosity or Reynolds stresses, such as in Reynolds-Averaged Navier-Stokes (RANS) models, but instead to re-calibrate the Boltzmann model to the characteristic time scales of a turbulent flow motion. This constitutes the essence of the LBM-VLES approach. Furthermore, to reduce the computational cost deriving from the use of uniform Cartesian grid near solid walls, a pressure-gradient-extended wall-model [44] is used to approximate the no-slip boundary condition.

IV. Numerical setup

A. Aircraft Geometry

The aircraft geometry consists of the strut-braced wing developed in the initial phase of the Clean Aviation project HERWINGT, and the fuselage designed in the parent project HERA. The wing is the result of an aerodynamic optimization performed through the *in-house* optimization framework WiMOT (Wing Multiobjective Optimization Tool). The optimization framework is based on a gradient-free algorithm and on low/mid-fidelity CFD methods. Specifically, the aerodynamic performances are computed by combining the span-wise lift distribution obtained using a Vortex Lattice Method, [45], and the sectional drag force obtained using a compressible Viscous/Inviscid Interaction Method, [46], in several sections along the wing-span; whereas the optimal condition is reached by means of a genetic

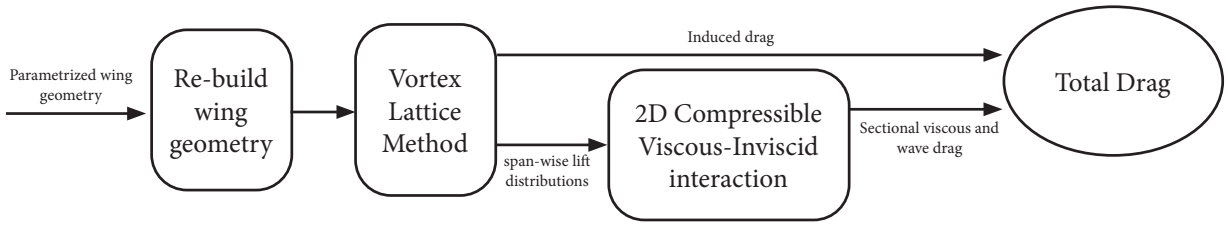

Fig. 1 WiMOT objective function flow chart.

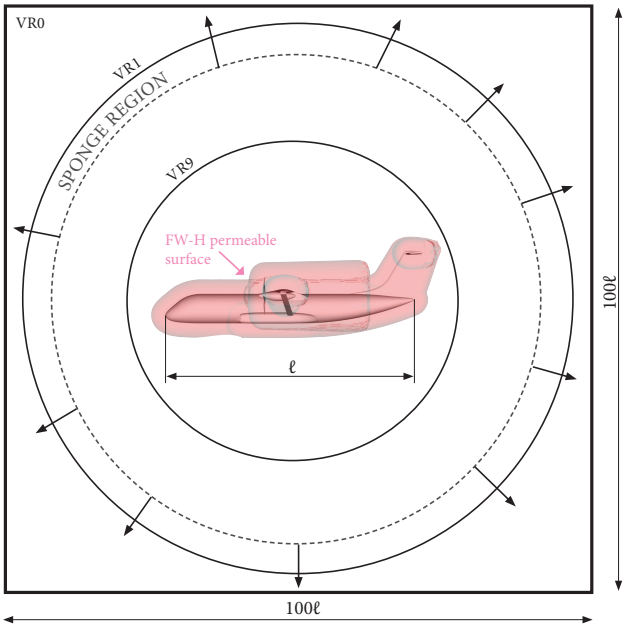

Fig. 2 Representation of the aircraft geometry and computational domain sketch. The domain boundaries and the resolution regions (VRs) are not drawn to scale.

algorithm. The objective function is shown in Fig. 1. The employed tool is therefore able to take into account the interaction between multiple lifting surfaces, laminar-to-turbulent transition and shock waves eventually occurring in the region enclosed by the wing and the strut. The framework relies on *Class Shape function Transformation* method [47] for the geometry parametrization.

Wing aspect ratio, AR, is 17 with a wing semi-span length $b = 17.62\,m$. The fuselage longitudinal length is $\ell = 30.75\,m$. Since the specific geometry of the propeller and nacelle are unavailable at the present stage of the project, the authors inferred their characteristics based on available preliminary design information. Thus, in this manuscript a six blades propeller with a disk diameter $d = 5.02\,m$ is used. The propeller angular speed is set to $RPM = 1103$ and the collective blade pith is trimmed at the analysed flight condition, specified in section IV.B, to obtain the desired thrust setting of $C_T = \rho n^2 D^4 T = 0.09$. Additionally, given the lack of details regarding high-lift devices, the focus of this study is solely on analyzing the clean configuration at high lift condition specified in the Section IV.B. The aircraft geometry used for computational purposes is depicted in Fig. 2.

B. Flight condition and solver settings

The simulations are performed at flight condition specified by

$$M_\infty = 0.20,\ h = 0\,m,\ Re_\infty/c = 4.6 \cdot 10^6\,1/m,\ AoA = 10\,deg. \tag{6}$$

The computational domain consists of 15 resolution regions (VRs). For simplicity and clarity drawing, only VR0,VR1 and VR9 are shown in Fig. 2. The VR from 2 to 8 are sphere uniformly distributed between VR1 and VR9.

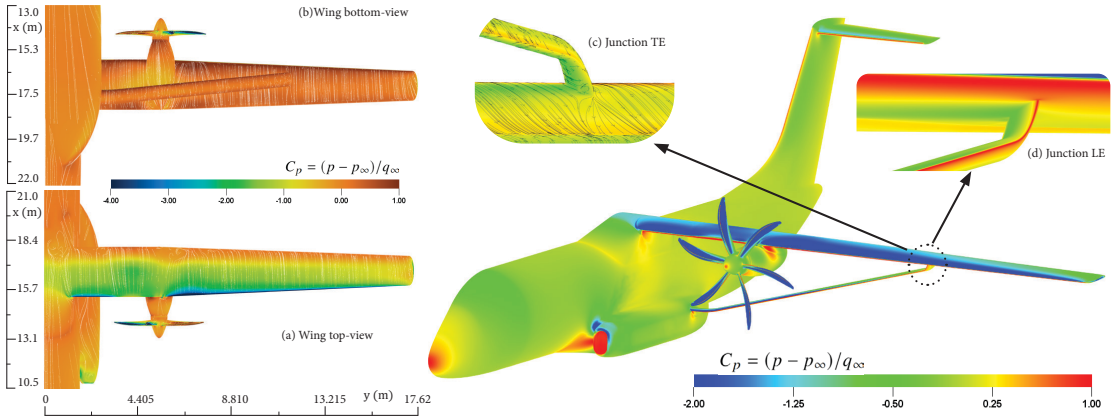

Fig. 3 Pressure coefficient distribution, $C_p = (p - p_\infty)/q_\infty$, on the aircraft surface. On the left, the top (a) and bottom (b) views of the wing. Surface streamlines are depicted in white. On the right, the pressure coefficient distribution is shown for the entire aircraft, focusing specifically on the strut-wing junction TE (c) and LE (d). Surface streamlines are displayed in black for the junction TE view.

Afterward, VR10 to 15 are defined as offset from the aircraft body to have higher resolution in the propeller wake and towards intersection regions between geometries, such as the strut-wing junction or the wing/strut-fuselage junction. Starting from the VR closest to the body, the grid size doubles when moving towards the outer VRs. A dedicated VR encompassing the propeller blades and the spinner is associated with a rotating reference frame at the propeller angular speed. An acoustic sponge region is specified, starting from a radius of 7.6ℓ from the aircraft center, to damp outward-travelling and inward-reflected acoustic waves. The far field boundary is located at 50 fuselage lengths as can be seen from Fig. 2. Turbulent boundary conditions are set on every surface except for the propeller blades in which trips are applied at 20% of the chord to force laminar-to-turbulent transition. For the case symmetry with respect to the Y plane, only half of the vehicle is simulated.

Far-field noise is computed using both solid and permeable surface formulations of the FWH acoustic analogy. The permeable surface, represented in Fig. 2, is defined as an offset from the aircraft surface, augmented with a cylindrical extrusion to prevent interference from the propeller wake. Three permeable surfaces 25 cm apart are used for averaging purpose [48]. Advanced time domain approach is employed to compute far-field noise.

V. Results

A. Averaged Flow Field

Fig. 3 shows the averaged pressure coefficient distribution on the aircraft surface. A region of separated flow is visible on the upper side of the wing from the 65% of chord around the span-wise coordinate $y = 5.5\,m$ (Fig. 3-(a)). This is likely due to an higher local angle of attack induced by the propeller wake in that region which is evidenced by the higher flow expansion observed on wing Leading Edge (LE) at the left of the propeller axis. Looking at the bottom view (Fig. 3-(b)), high flow expansion can be observed in the region between the nacelle and the strut due to the reduction of sectional area encountered by the flow. The same happens at the junction between the strut and wing (Fig. 3-(d)) although no sonic conditions are observed. Additionally, all the geometric intersection, including wing-nacelle, wing-fuselage, strut-fuselage and strut-wing, are affected by the flow separations. Specifically, in the wing top view (Fig. 3-(a)) a re-circulation region at the wing-fuselage intersection can be observed from the surface streamlines distribution. Eventually, as can be seen from the junction Trailing edge (TE) image in Fig. 3-(c), a corner separation appears at the trailing edge of the strut-wing connection.

An inspection of the pressure fluctuations induced by the flow is presented in Fig. 4 where the standard deviation of static pressure is displayed. It is clear that the highest pressure fluctuations occur in a region of separated flow on the aircraft sponson, at the geometric intersections, including strut-fuselage and wing-fuselage connection, and in the wake of the propeller. In addition, the standard deviation of pressure reveals the effect of the propeller slipstream on

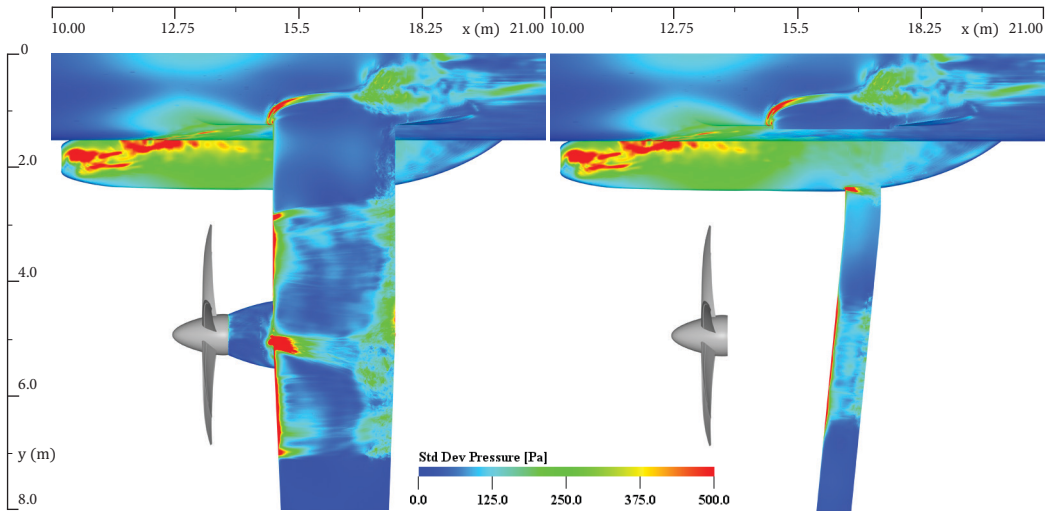

Fig. 4 Root mean square of the acoustic pressure on the wing top side (left) and on the strut (right). For clarity purpose the wing and the nacelle have been hidden to generate the image on the right.

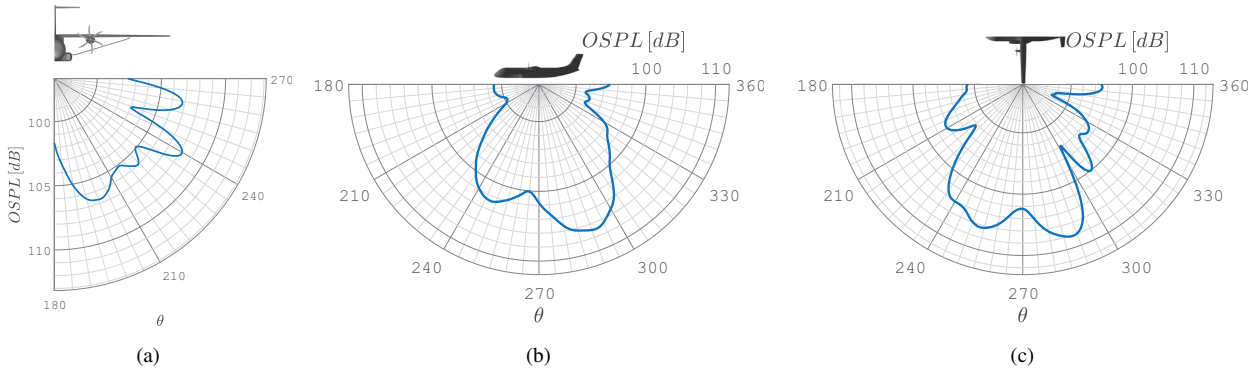

Fig. 5 Overall Sound Pressure Level in the frontal plane (a), lateral plane (b) and top plane (c).

at the LE of both wing and strut. Specifically, the pressure fluctuation on the wing are more intense at the edges of the impingement region, indicating that the most critical interaction occurs with the tip vortex of the blades (as also found in a study of propeller-pylon interaction [49]). Compared to the wing, the impingement region on the strut is less extended in the span-wise direction because of the strut inclination angle and position with respect of the propeller. In addition, around the center of the impingement region, where the wing kink separates its straight and swept sections, a region of high-pressure fluctuations can also be observed. This phenomenon is not related to the propeller slipstream but arises from flow separation at the nacelle-wing intersection, propagating downstream and impacting the flow field on the wing.

B. Far-field analysis

Fig. 5 illustrates directivity plots in various aircraft planes, with a circular microphone array positioned 50 meters from the aircraft center. Looking at the lateral plane Fig. 5-(b) and the top plane Fig. 5-(c), predominant lobes can be observed between $\theta = 240 - 300°$. Conversely, in the frontal plane (Fig. 5-(a)) no primary lobes are discernible and the noise is radiated almost uniformly. Frequency spectra are computed and displayed in Fig. 6 in terms of the Blade Passing Frequency (BPF) for each of these planes. These spectra reveal narrow-band structure with multiple tones at the BPF and its harmonics, indicating that most of the far-field noise originates from the propeller and from the reflections of its acoustic waves on the aircraft surfaces.

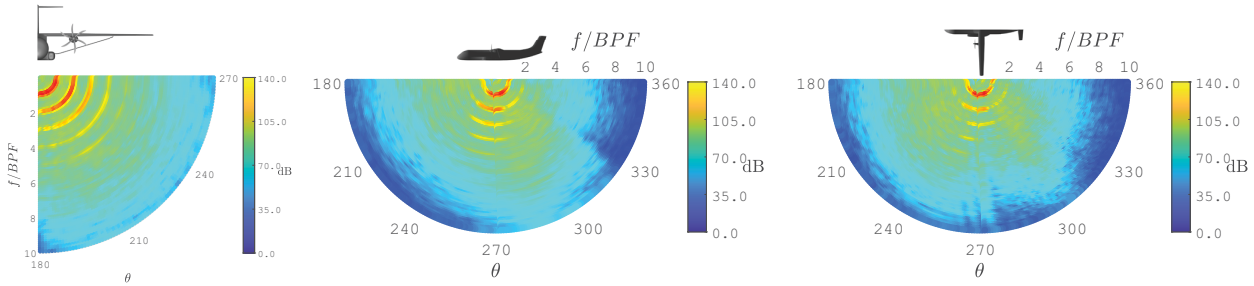

(a) (b) (c)

Fig. 6 Frequency spectra directivity plot in the frontal plane (a), lateral plane (b) and top plane (c). The frequency is scaled by the Blade Passing Frequency (BPF).

C. Noise sources identification

To identify the noise sources the Dassault software *optydb_pfnoisescan* is employed. Although the analysis may depend on the microphone's location, a representative microphone has been selected to perform noise sources identification. The chosen microphone is located at 50 m distance from the airplane in the frontal plane in the middle angular range (i.e. at 45 *deg* with respect to the vertical axis). For this microphone location the acoustic pressure on the aircraft surface which contributes to the far-field sound has been computed and the results are shown in Fig. 7 in terms of acoustic pressure per unit area. It can be seen that the propeller, the wing, the strut, the sponson and the junctions, where flow separation was observed in Section V.A, are the main contributor to far-field sound. To identify the principal frequencies of the signal scattering from the different aircraft component, the Power Spectral Density (PSD) is computed using a solid FWH approach and displayed in Fig. 8. The wing and the strut show tones at first and second BPF. Moreover, while the wing presents almost the same tones at those frequencies, the strut tone contributes higher values at the second BPF. The constructive pressure contribution at the BPF and at twice the BPF are illustrated in Fig. 9 and 10, respectively. This constructive term represents the local FWH surfel contribution in-phase with the total far-field noise at the specified frequency band [50]. It can be seen that the highest noise source is the propeller as it is also clear from the PSD diagram in Fig.8. Strong contribution at this frequency is given by the reflection of the acoustic wave generated by the propeller on the fuselage sponson which is not directly related to the SBW configuration. Further constructive contribution is produced in the region where the slipstream impinges. Specifically the noise is generated in the region delimited by the wing lower surface and strut upper surface and the intensity of this noise source is shown to be more relevant at a frequency equal to twice the BPF. No relevance at these frequencies is shown for the junction separations observed in Fig. 7.

VI. Conclusion

The aeroacoustic properties of a propeller-driven aircraft with a strut-braced wing have been analysed in high-lift condition focusing on the clean wing geometry (without H-L devices). It has been shown that the most significant contributors to surface pressure fluctuations are the multiple geometric intersections and the interaction between the propeller wake and the wing and strut leading edges.

Far-field noise analysis through permeable surface FWH formulation showed that the noise emitted from the aircraft radiates mainly in the bottom-lateral direction at the BPF and its harmonics. Also, broadband contribution at the higher frequencies is observed. Noise source identification conducted through a solid FWH analysis has been presented. The analysis revealed that the effect of interaction between the wing, the strut and the propeller slipstream results in a strong additional far-field noise contribution at twice the Blade Passing Frequency. Furthermore, this noise scatters specifically from the region bounded by the wing's lower surface and the strut's upper surface.

These results emphasize that while introducing multiple surfaces can improve aerodynamics, it can also exacerbate aeroacoustics by adding noise sources such as geometric intersections and potential propeller slipstream interactions. Therefore, caution is essential during the design phase of such promising non-conventional aircraft configurations and effort should be made to assess their acoustic impact. Eventually, the current study does not delve into the investigation of broadband sources, which will be the focus of future research endeavors by the authors.

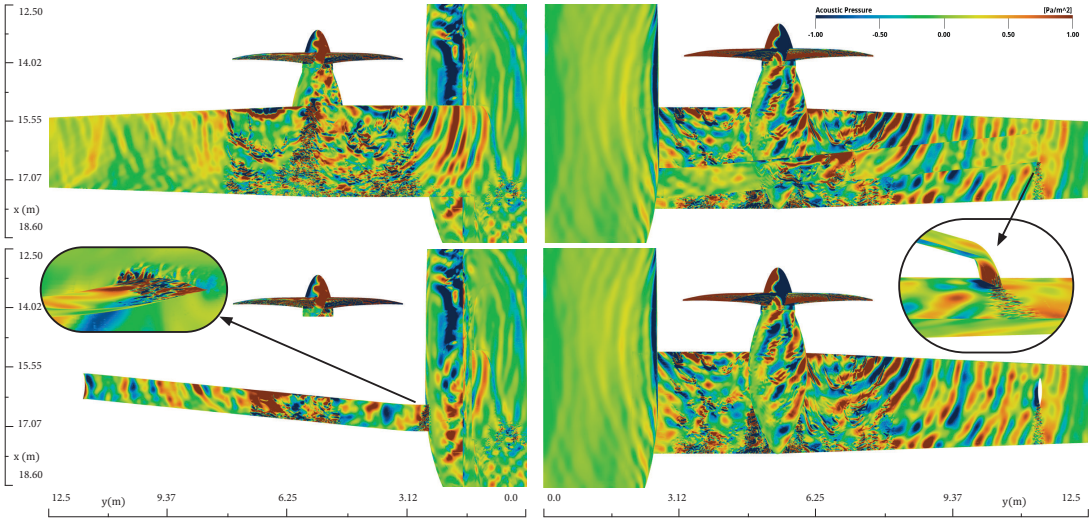

Fig. 7 Acoustic Pressure per unit of area. The top-left image depicts the wing's upper side distribution, while the bottom-left image reveals the upper side of the strut and fuselage sponson by hiding the wing and nacelle. A focus on the wing-fuselage intersection is also included. On the top-right, the lower side of the strut is illustrated, whereas the bottom-right image displays the wing's underside by hiding the strut surface. A focus on the strut-wing junction TE is also included.

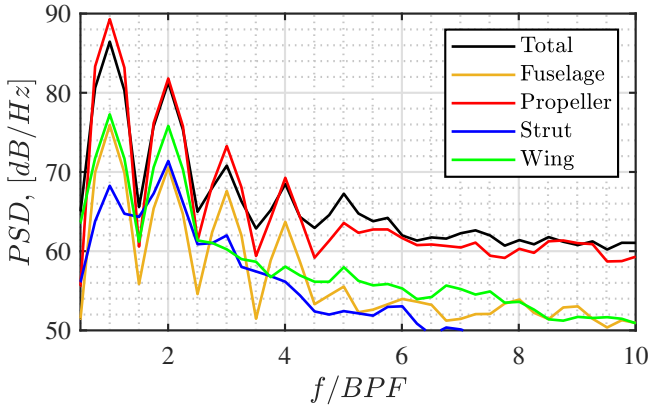

Fig. 8 Power Spectral Density (PSD) obtained through solid FWH formulation.

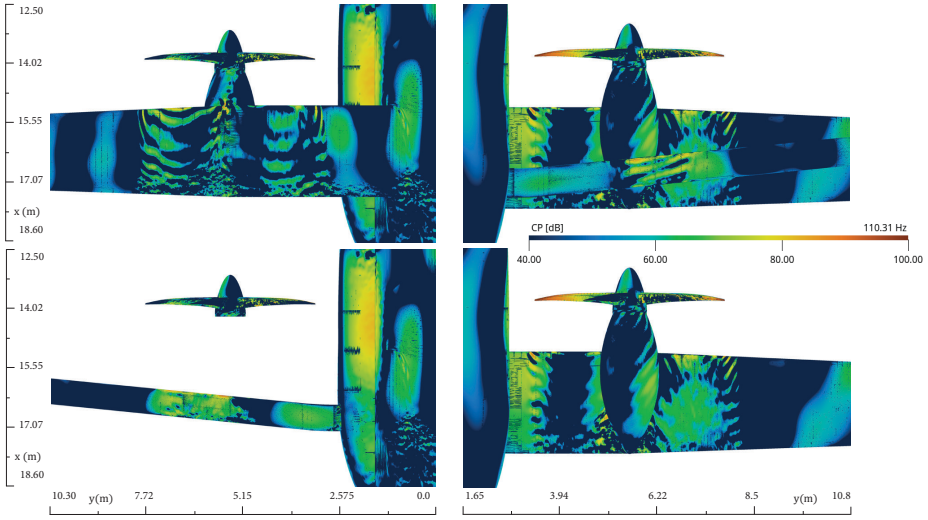

Fig. 9 Surface acoustic pressure distribution contributing to far-field Noise at frequency band centered at the BPF, visualized using Dassault Systems *optydb_pfnoisescan* software. The top-left image depicts the wing's upper side distribution, while the bottom-left image reveals the upper side of the strut and fuselage sponson by hiding the wing and nacelle. On the top-right, the lower side of the strut is illustrated, whereas the bottom-right image displays the wing's underside by hiding the strut surface.

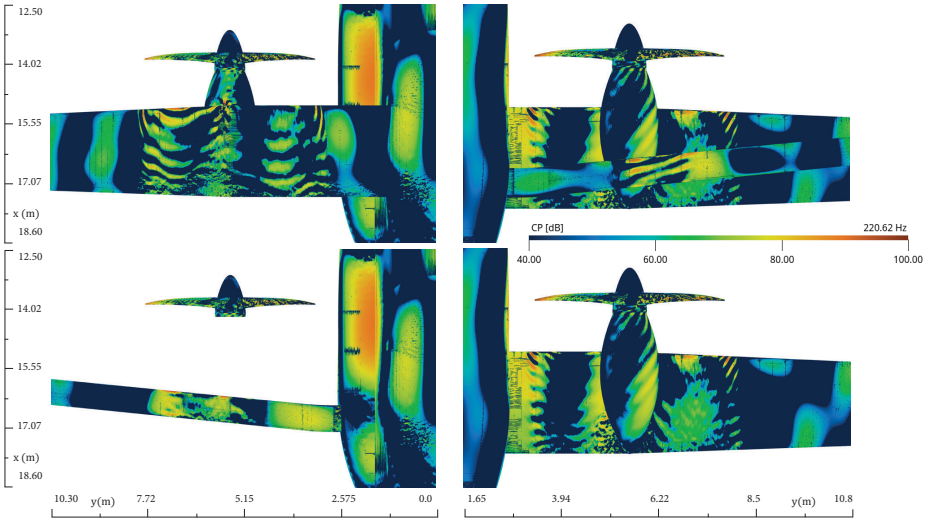

Fig. 10 Surface acoustic pressure distribution contributing to far-field Noise at frequency band centered at 2 times the BPF, visualized using Dassault Systems *optydb_pfnoisescan* software. The top-left image depicts the wing's upper side distribution, while the bottom-left image reveals the upper side of the strut and fuselage sponson by hiding the wing and nacelle. On the top-right, the lower side of the strut is illustrated, whereas the bottom-right image displays the wing's underside by hiding the strut surface.

Acknowledgments

The authors gratefully acknowledge financial support from the Clean Aviation Joint Undertaking under the HERWINGT project (grant agreement No. 101102010). The granting authority receives support from the European Union's Horizon Europe research and innovation program and the Clean Aviation Joint Undertaking members other than the Union. Views and opinions expressed are however those of the author(s) only and do not necessarily reflect those of the European Union or Clean Aviation Joint Undertaking. Neither the European Union nor the granting authority can be held responsible for them.

References

[1] Aviation, C., "Strategic Research and Innovation Agenda 2021," Tech. rep., 2021. URL https://www.clean-aviation.eu/strategic-research-and-innovation-agenda-sria.

[2] European Commission, *Communication from the commission to the European Parliament, the Council, the European Econominc and Social Committee of the regions: Stepping up Europe's 2030 climate ambition Investing in a climate-neutral future for the benefit of our people*, An action plan from the European Commission, 2020. URL https://eur-lex.europa.eu/legal-content/EN/TXT/?uri=CELEX:52020DC0562, (Report COM/2020/562 final).

[3] Kroo, I., "DRAG DUE TO LIFT: Concepts for Prediction and Reduction," *Annual Review of Fluid Mechanics*, Vol. 33, No. 1, 2001, pp. 587–617. https://doi.org/10.1146/annurev.fluid.33.1.587.

[4] Martins, J. R. R. A., Kennedy, G., and Kenway, G. K., *High Aspect Ratio Wing Design: Optimal Aerostructural Tradeoffs for the Next Generation of Materials*, 2014. https://doi.org/10.2514/6.2014-0596.

[5] Chau, T., and Zingg, D. W., "Aerodynamic Design Optimization of a Transonic Strut-Braced-Wing Regional Aircraft," *Journal of Aircraft*, Vol. 59, No. 1, 2022, pp. 253–271. https://doi.org/10.2514/1.C036389.

[6] Boyne, W. J., "The Hurel-Dubois and Maurice Hurel," https://www.historynet.com/the-hurel-dubois-and-maurice-hurel/, 2006. [Online; accessed 20-April-2024].

[7] Wikipedia contributors, "Hurel-Dubois HD.10 — Wikipedia, The Free Encyclopedia," https://en.wikipedia.org/w/index.php?title=Hurel-Dubois_HD.10&oldid=1141375225, 2023. [Online; accessed 20-April-2024].

[8] Wikipedia contributors, "Short C-23 Sherpa — Wikipedia, The Free Encyclopedia," , 2023. URL https://en.wikipedia.org/w/index.php?title=Short_C-23_Sherpa&oldid=1167603871, [Online; accessed 3-August-2023].

[9] Droney, C. K., Sclafani, A. J., Harrison, N. A., Grasch, A. D., and Beyar, M. D., "Subsonic Ultra Green Aircraft Research: Phase III-Mach 0.75 Transonic Truss-Braced Wing Design," , 2020. URL https://ntrs.nasa.gov/api/citations/20205005698/downloads/NASACR20205005698_0208%20PUBLIC-rev2.pdf.

[10] Carrier, G., Atinault, O., Dequand, S., Hantrais-Gervois, J.-L., Liauzun, C., Paluch, B., A.-M., Rodde, Toussaint, C., and Onera, "INVESTIGATION OF A STRUT-BRACED WING CONFIGURATION FOR FUTURE COMMERCIAL TRANSPORT," 2012. URL https://www.icas.org/ICAS_ARCHIVE/ICAS2012/PAPERS/597.PDF.

[11] Moerland, E., Pfeiffer, T., Böhnke, D., Jepsen, J., Freund, S., Liersch, C. M., Chiozzotto, G. P., Klein, C., Scherer, J., Hasan, Y. J., and Flink, J., *On the Design of a Strut-Braced Wing Configuration in a Collaborative Design Environment*, 2017. https://doi.org/10.2514/6.2017-4397.

[12] Gur, O., Schetz, J. A., and Mason, W. H., "Aerodynamic Considerations in the Design of Truss-Braced-Wing Aircraft," *Journal of Aircraft*, Vol. 48, No. 3, 2011, pp. 919–939. https://doi.org/10.2514/1.C031171.

[13] Grasmeyer, J. M., Naghshineh-Pour, A., Tetrault, P.-A., Grossman, B., Haftka, R. T., Kapania, R. K., Mason, W. H., and Schetz, J. A., "Multidisciplinary Design Optimization of a Strut-Braced Wing Aircraft with Tip-Mounted Engines," 1998.

[14] Gundlach, J. F., Tétrault, P.-A., Gern, F., Nagshineh-Pour, A., Ko, A., Schetz, J. A., Mason, W. H., Kapania, R., Grossman, B., and Haftka, R. T., "AIAA 2000-0420 Multidisciplinary Design Optimization of a Strut-Braced Wing Transonic Transport," 2020.

[15] Gundlach, J. F., Tetrault, P.-A., Gern, F. H., Nagshineh-Pour, A. H., Ko, A., Schetz, J. A., Mason, W. H., Kapania, R. K., Mason, W. H., Grossman, B., and Haftka, R. T., "Conceptual Design Studies of a Strut-Braced Wing Transonic Transport," *Journal of Aircraft*, Vol. 37, No. 6, 2000, pp. 976–983.

[16] Gern, F. H., Ko, A., Sulaeman, E., Gundlach, J. F., Kapania, R. K., and Haftka, R. T., "Multidisciplinary design optimization of a transonic commercial transport with strut-braced wing," *Journal of Aircraft*, Vol. 38, 2001, pp. 1006–1014. https://doi.org/10.2514/2.2887.

[17] Seber, G., Ran, H., Schetz, J. A., and Mavris, D. N., "Multidisciplinary Design Optimization of a Truss Braced Wing Aircraft with Upgraded Aerodynamic Analyses," 2011.

[18] Meadows, N. A., Schetz, J. A., Kapania, R. K., Bhatia, M., and Seber, G., "Multidisciplinary Design Optimization of Medium-Range Transonic Truss-Braced Wing Transport Aircraft," *Journal of Aircraft*, Vol. 49, No. 6, 2012, pp. 1844–1856. https://doi.org/10.2514/1.C031695.

[19] "Comparative assessment of strut-braced and truss-braced wing configurations using multidisciplinary design optimization," American Institute of Aeronautics and Astronautics Inc., 2015, pp. 2009–2020.

[20] Secco, N. R., and Martins, J. R. R. A., "RANS-Based Aerodynamic Shape Optimization of a Strut-Braced Wing with Overset Meshes," *Journal of Aircraft*, Vol. 56, No. 1, 2019, pp. 217–227. https://doi.org/10.2514/1.C034934.

[21] Chau, T., and Zingg, D., "Fuel burn evaluation of a transonic strut-braced-wing regional aircraft through multipoint aerodynamic optimisation," *The Aeronautical Journal*, Vol. 127, No. 1308, 2023, p. 305–329. https://doi.org/10.1017/aer.2022.64.

[22] Carrier, G., Arnoult, G., Fabbiane, N., Schotté, J.-S., David, C., Defoort, S., Delavenne, M., and Bénard, E., "Multidisciplinary analysis and design of strut-braced wing concept for medium range aircraft," , 2022. URL https://hal.science/hal-03664145.

[23] Filippone, A., "Aircraft noise prediction," *Progress in Aerospace Sciences*, Vol. 68, 2014, pp. 27–63. https://doi.org/https://doi.org/10.1016/j.paerosci.2014.02.001.

[24] Simpson, R. L., "JUNCTION FLOWS," *Annual Review of Fluid Mechanics*, Vol. 33, No. 1, 2001, pp. 415–443. https://doi.org/10.1146/annurev.fluid.33.1.415.

[25] Owens, D. E., "Wall Features of Wing-Body Junctions: Towards Noise Reduction," Master thesis, Virginia Tech, 08 2013.

[26] Ding, Y., Zhang, T., Geyer, T. F., de Silva, C. M., Doolan, C. J., and Moreau, D. J., "Experimental Investigation of the Flow Characteristics and Noise Generation at the Wing–Wall Junction," *Journal of Aerospace Engineering*, Vol. 34, No. 5, 2021, p. 04021054. https://doi.org/10.1061/(ASCE)AS.1943-5525.0001303.

[27] Teruna, C., Rego, L., Casalino, D., Avallone, F., and Ragni, D., "A Numerical Study on Aircraft Noise Mitigation Using Porous Stator Concepts," *Aerospace*, Vol. 9, No. 70, 2022.

[28] Romani, G., Ye, Q., Avallone, F., Ragni, D., and Casalino, D., "Numerical analysis of fan noise for the NOVA boundary-layer ingestion configuration," *Aerospace Science and Technology*, Vol. 96, 2020, p. 105532. https://doi.org/https://doi.org/10.1016/j.ast.2019.105532.

[29] Casalino, D., van der Velden, W., and Romani, G., "Community Noise of Urban Air Transportation Vehicles," *AIAA Paper 2019-1834*, 2019.

[30] Avallone, F., Casalino, D., and Ragni, D., "Impingement of a Propeller Slipstream on a Leading Edge with a Flow-Permeable Insert: A Computational Aeroacoustic Study," *International Journal of Aeroacoustics*, Vol. 17, No. 6-8, 2018.

[31] Romani, G., and Casalino, D., "Rotorcraft Blade-Vortex Interaction Noise Prediction using the Lattice-Boltzmann Method," *Aerospace Science and Technology*, Vol. 800, 2019, pp. 147–157.

[32] Lockard, D., Humphreys, W., Khorrami, M., Fares, E., Casalino, D., and Ravetta, P., "Comparison of Computational and Experimental Microphone Array Results for an 18%-Scale Aircraft Model," *International Journal of Aeroacoustics*, Vol. 16, No. 4-5, 2017, pp. 358–381.

[33] Hazir, A., and Casalino, D., "Lattice Boltzmann Based Aeroacoustic Simulation of Turbofan Noise Installation Effects," *Proceedings of the 23rd International Congress on Sound and Vibration, Athens, Greece*, 2016.

[34] Fares, E., Casalino, D., and Khorrami, M., "Evaluation of Airframe Noise Reduction Concepts via Simulations Using a Lattice Boltzmann Approach," *AIAA Paper 2015-2988*, 2015.

[35] Khorrami, M. R., Fares, E., and Casalino, D., "Towards Full Aircraft Airframe Noise Prediction: Lattice Boltzmann Simulations," *AIAA Paper 2014-2481*, 2014.

[36] Cerizza, D., Casalino, D., and Gonzalez-Martino, I., "An Extension of the Acoustics Evaluation of the NASA SDT Turbofan with Lattice-Boltzmann Methods," *AIAA Paper 2022-2886*, 2022.

[37] Casalino, D., Avallone, F., Gonzalez-Martino, I., and Ragni, D., "Aeroacoustic Study of a Wavy Stator Leading Edge in a Realistic Fan/OGV Stage," *Journal of Sound and Vibration*, Vol. 442, 2019, pp. 138–154.

[38] Gonzalez-Martino, I., and Casalino, D., "Fan Tonal and Broadband Noise Simulations at Transonic Operating Conditions Using Lattice-Boltzmann Methods," *AIAA Paper 2018-3919*, 2018.

[39] Casalino, D., Hazir, A., and Mann, A., "Turbofan Broadband Noise Prediction using the Lattice Boltzmann Method," *AIAA Journal*, Vol. 56, No. 2, 2017. https://doi.org/10.2514/1.J055674.

[40] Bhatnagar, P. L., Gross, E. P., and Krook, M., "A Model for Collision Processes in Gases. I. Small Amplitude Processes in Charged and Neutral One-Component Systems," *Phys. Rev.*, Vol. 94, 1954, pp. 511–525. https://doi.org/10.1103/PhysRev.94.511, URL https://link.aps.org/doi/10.1103/PhysRev.94.511.

[41] Chen, H., Chen, S., and Matthaeus, W. H., "Recovery of the Navier-Stokes equations using a lattice-gas Boltzmann method," *Phys. Rev. A*, Vol. 45, 1992, pp. R5339–R5342. https://doi.org/10.1103/PhysRevA.45.R5339, URL https://link.aps.org/doi/10.1103/PhysRevA.45.R5339.

[42] CHEN, H., ORSZAG, S. A., STAROSELSKY, I., and SUCCI, S., "Expanded analogy between Boltzmann kinetic theory of fluids and turbulence," *Journal of Fluid Mechanics*, Vol. 519, 2004, p. 301–314. https://doi.org/10.1017/S0022112004001211.

[43] Yakhot, V., and Orszag, S. A., "Renormalization group analysis of turbulence. I. Basic theory," *Journal of Scientific Computing*, Vol. 1, No. 1, 1986, p. 3–51. https://doi.org/10.1007/bf01061452, URL https://doi.org/10.1007/bf01061452.

[44] Teixeira, C., "INCORPORATING TURBULENCE MODELS INTO THE LATTICE-BOLTZMANN METHOD," *International Journal of Modern Physics C*, Vol. 09, 1998, pp. 1159–1175. URL https://api.semanticscholar.org/CorpusID:120645561.

[45] Drela, M. and Youngren, H., "Athena Vortex Lattice," http://web.mit.edu/drela/Public/web/avl/, Accessed: 2023-12-01, 2023.

[46] Drela, M., "MSES - Software for High-Lift Multi-element Airfoil Configuration," http://web.mit.edu/drela/Public/web/mses/, Accessed: 2023-12-01, 2023.

[47] Kulfan, B. M., "Universal Parametric Geometry Representation Method," *Journal of Aircraft*, Vol. 45, No. 1, 2008, pp. 142–158. https://doi.org/10.2514/1.29958.

[48] Mendez, S., Shoeybi, M., Lele, S. K., and Moin, P., "On the Use of the Ffowcs Williams-Hawkings Equation to Predict Far-Field Jet Noise from Large-Eddy Simulations," *International Journal of Aeroacoustics*, Vol. 12, No. 1-2, 2013, pp. 1–20. https://doi.org/10.1260/1475-472X.12.1-2.1.

[49] Sinnige, T., de Vries, R., Corte, B. D., Avallone, F., Ragni, D., Eitelberg, G., and Veldhuis, L. L. M., "Unsteady Pylon Loading Caused by Propeller-Slipstream Impingement for Tip-Mounted Propellers," *Journal of Aircraft*, Vol. 55, No. 4, 2018, pp. 1605–1618. https://doi.org/10.2514/1.C034696.

[50] Casalino, D., Romani, G., Pii, L. M., and Colombo, R., "Flow confinement effects on sUAS rotor noise," *Aerospace Science and Technology*, Vol. 143, 2023, p. 108756. https://doi.org/https://doi.org/10.1016/j.ast.2023.108756.